Sub-Micrometer Phonon Mean Free Paths in Metal−Organic Frameworks Revealed by Machine Learning Molecular Dynamics Simulations

Penghua Ying,* Ting Liang, Ke Xu, Jin Zhang, Jianbin Xu, Zheng Zhong, and Zheyong Fan*
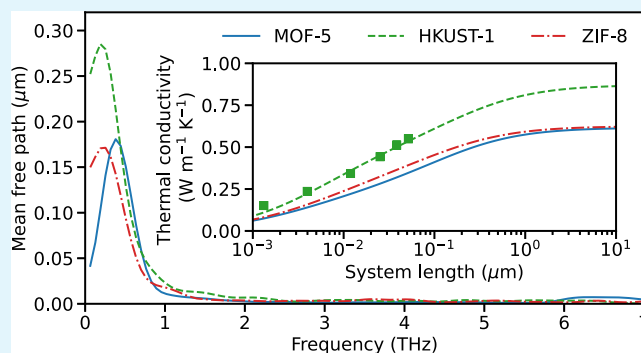
ACCESS | Metrics & More | Article Recommendations | Supporting Information

ABSTRACT: Metal−organic frameworks (MOFs) are a family of materials that have high porosity and structural tunability and hold great potential in various applications, many of which require a proper understanding of the thermal transport properties. Molecular dynamics (MD) simulations play an important role in characterizing the thermal transport properties of various materials. However, due to the complexity of the structures, it is difficult to construct accurate empirical interatomic potentials for reliable MD simulations of MOFs. To this end, we develop a set of accurate yet highly efficient machine-learned potentials for three typical MOFs, including MOF-5, HKUST-1, and ZIF-8, using the neuroevolution potential approach as implemented in the GPUMD package, and perform extensive MD simulations to study thermal transport in the three MOFs. Although the lattice thermal conductivity values of the three MOFs are all predicted to be smaller than 1 W/(m K) at room temperature, the phonon mean free paths (MFPs) are found to reach the sub-micrometer scale in the low-frequency region. As a consequence, the apparent thermal conductivity only converges to the diffusive limit for micrometer single crystals, which means that the thermal conductivity is heavily reduced in nanocrystalline MOFs. The sub-micrometer phonon MFPs are also found to be correlated with a moderate temperature dependence of thermal conductivity between those in typical crystalline and amorphous materials. Both the large phonon MFPs and the moderate temperature dependence of thermal conductivity fundamentally change our understanding of thermal transport in MOFs.

KEYWORDS: metal−organic frameworks, thermal conductivity, phonon mean free paths, machine-learned potential, molecular dynamics simulations

INTRODUCTION

In the last two decades, due to their ultra-high porosity[1] and structural tunability,[2] metal−organic frameworks (MOFs) have shown great potential in various applications, such as gas storage and separation,[3] water harvesting,[4] electronic devices,[5] and heterogeneous catalysis.[6] Lattice thermal conductivity is a critical parameter for MOFs in the context of thermal energy conversion, thermal management, and thermal stability and has attracted extensive experimental[7−11] and theoretical[12−27] studies.

It is generally difficult to produce large-scale single crystals of MOFs, which then usually exist in the form of powders. The small crystalline sizes present a great challenge for experimentally measuring the thermal conductivity of MOF crystals[9] because the contact thermal resistance between the crystalline particles can introduce large systematic errors. Despite this, single-crystalline MOF-5[28] can be grown up to a linear dimension of a couple of millimeters, and its thermal conductivity has been measured to be 0.32 W/(m K)[7] using the steady-state direct method. Recent advances in exper-
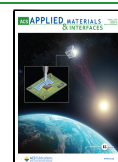
imental techniques also enabled the measurement of the thermal conductivity of a few typical MOFs in single-crystal form. For example, the thermal conductivity of single-crystal ZIF-8[29] was measured to be 0.64 ± 0.09 W/(m K) using the Raman-resistance temperature detector method.[10] For HKUST-1,[30] a value of 0.69 ± 0.05 W/(m K) was determined based on the thermoreflectance method.[11]

Computationally, molecular dynamics (MD) simulation has played an important role in calculating the lattice thermal conductivity and revealing the underlying mechanics for thermal transport in MOFs. Both the equilibrium molecular dynamics (EMD)[31,32] and the nonequilibrium molecular

dynamics (NEMD) methods have been extensively used. However, results from these two methods seem to be conflicting. For example, a weak temperature dependence of thermal conductivity in MOF-5 has been predicted using EMD simulations, which was attributed to short phonon mean free paths (MFPs) on the order of the lattice parameter.[12] Similarly, for ZIF-4 and ZIF-62, it has been suggested, based on EMD simulations,[24,25] that the phonon transport are strongly localized with phonon MFPs less than 1.5 nm. However, recent NEMD simulations suggested that the thermal conductivity of MOF-5 is actually not fully converged even when the transport length exceeds 20 nm[23,26] and phonons with MFPs larger than 100 nm exist in HKUST-1.[27]

The differences in the results could be partially attributed to the different interatomic potentials used in different works, but there are two other possible causes. On the one hand, the heat current as implemented in the LAMMPS package[34] used in most of the previous EMD simulations[13,14,17−20,24,25] was incorrect for many-body potentials, which could lead to significantly reduced thermal conductivity and phonon MFPs in systems with low-dimensional features.[35] On the other hand, it is often assumed that a supercell with $2 \times 2 \times 2$ conventional cells is sufficient to obtain convergent results in EMD simulations,[12−14,17,19,20,36] which is not necessarily valid. It is important to resolve the conflict between the EMD and the NEMD methods and obtain a clear and consistent picture of the phonon MFPs in MOFs because phonon MFPs determine the variation of the apparent thermal conductivity with respect to the sample length, which, in the context of MOFs, can be the grain size of polycrystals or the linear size of the clusters in MOF powders.

In this paper, we present a coherent understanding of the phonon MFPs in MOFs by considering three typical MOFs, including MOF-5,[28] HKUST-1,[30] and ZIF-8,[29] as shown in Figure 1. To this end, we construct accurate interatomic potentials for these materials by training state-of-the-art machine-learned potentials (MLPs) against quantum-mechanical density functional theory (DFT) calculations. Recently, MLPs have been successfully applied to study a variety of properties of MOFs such as mechanical properties,[37] phase transition,[38] and gas diffusion.[39,40] Herein, we choose to use the neuroevolution potential (NEP) approach[41−43] that has been demonstrated to be highly efficient while being also sufficiently accurate. Moreover, the NEP approach has been implemented in the GPUMD package,[44] which has the correct implementation of the heat current.[35] We perform large-scale MD simulations to study thermal transport, establishing a coherent picture of thermal transport in MOFs by using three MD methods, including the aforementioned EMD and NEMD and a third one, namely, the homogeneous nonequilibrium molecular dynamics (HNEMD) method.[45] Our results show that in all of the three MOFs, the phonon MFPs can reach the sub-micrometer scale in the low-frequency region, which indicates that the thermal conductivity will be significantly reduced in polycrystals or powders with nanometer-scale grain sizes.

RESULTS AND DISCUSSION

Performance Evaluation of the NEP Models. We employed an iterative approach to develop machine-learned NEP models, as illustrated in Figure S1 (see Reference Data Generation Section for details). The NEP models for all of the three MOFs achieve very high accuracy, with root-mean-square
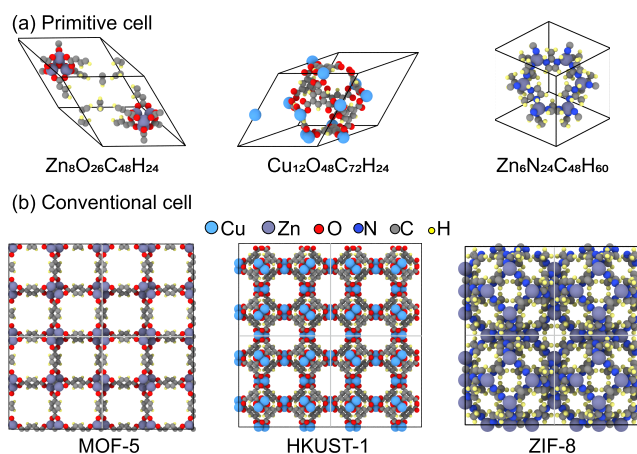

Figure 1. (a) Primitive and (b) $2 \times 2 \times 2$ conventional cells of MOF-5 (left), HKUST-1 (middle), and ZIF-8 (right). The primitive cells contain 106, 156, and 138 atoms, and the $2 \times 2 \times 2$ conventional ones contain 3992, 4992, and 2208 atoms. MOF-5[28] is formed by connecting Zn_4O clusters with 1,4-benzenedicarboxylate organic linkers, resulting in a primitive cubic net topology. HKUST-1[30] features copper paddle wheel units connected by 1,3,5-benzenetricarboxylate organic linkers, creating a body-centered cubic net topology. Lastly, ZIF-8[29] comprises tetrahedral ZnN_4 nodes connected by 2-methylimidazolate organic linkers, generating a sodalite net topology. We use primitive cells to prepare the reference data sets for training. For the calculation of thermal conductivity in MD simulations, we employ conventional cells of various system sizes. The OVITO package[33] was used for visualization.

errors (RMSEs) of energy, force, and virial being less than 0.6 meV/atom, 60 meV/Å, and 5 meV/atom, respectively, for both the training and test data sets (see Figure S2 and Table S1 for details). The zero-temperature lattice constants predicted by the NEP models closely match those predicted by DFT calculations, with a relative error being less than 0.1% (see Table S2 for details).

To further evaluate the accuracy of the NEP models in MD simulations, we compare the radial distribution functions and angular distribution functions of the three MOFs at 300 K calculated from the NEP models with those obtained from DFT and a few representative existing force fields (see Figure 2). The selected force fields include MOF-FF,[49] UFF4MOF,[46] and ReaxFF,[54] which have been widely used in MD simulation of the thermodynamics of MOF-5,[48] HKUST-1,[55] and ZIF-8.[19]

For radial distribution functions, we considered the most important pairs at the metal-linker interfaces: Zn−O in MOF-5, Cu−O in HKUST-1, and Zn−N in ZIF-8. Accordingly, we considered the O−Zn−O, O−Cu−O, and N−Zn−N triplets for the angular distribution functions. For both radial distribution functions and angular distribution functions, NEP achieves excellent agreement with DFT, while the existing force fields exhibit varying degrees of discrepancies compared to DFT. Among the three selected existing force fields, MOF-FF achieves the highest accuracy, and the other two are much less accurate. UFF4MOF predicts inaccurate positions for some radial distribution function peaks and too sharp peaks in the angular distribution functions, while ReaxFF predicts a nonexisting peak in the radial distribution function of MOF-5 and too flat angular distribution function of ZIF-8. The inaccuracies of ReaxFF in MD simulations of ZIFs have also been highlighted elsewhere.[56]
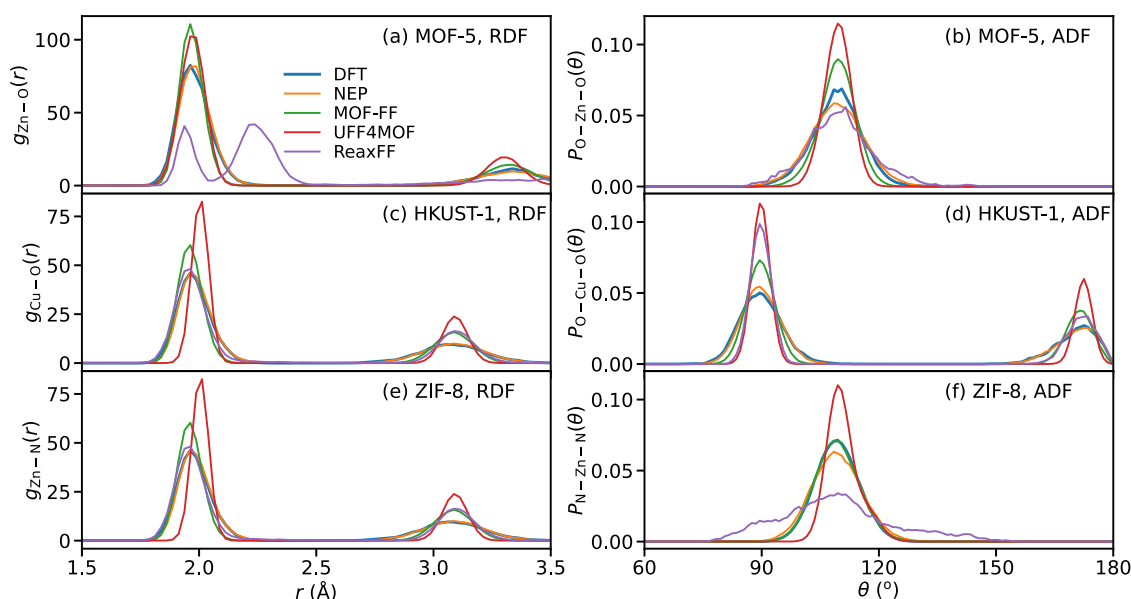
Figure 2. Typical radial distribution functions (labeled as RDF, left) and angular distribution functions (labeled as ADF, right) in (a, b) MOF-5, (c, d) HKUST-1, and (e, f) ZIF-8 calculated using classical MD simulations at 300 K driven by DFT, NEP, UFF4MOF,[46,47] MOF-FF,[48−50] and ReaxFF.[51−53]
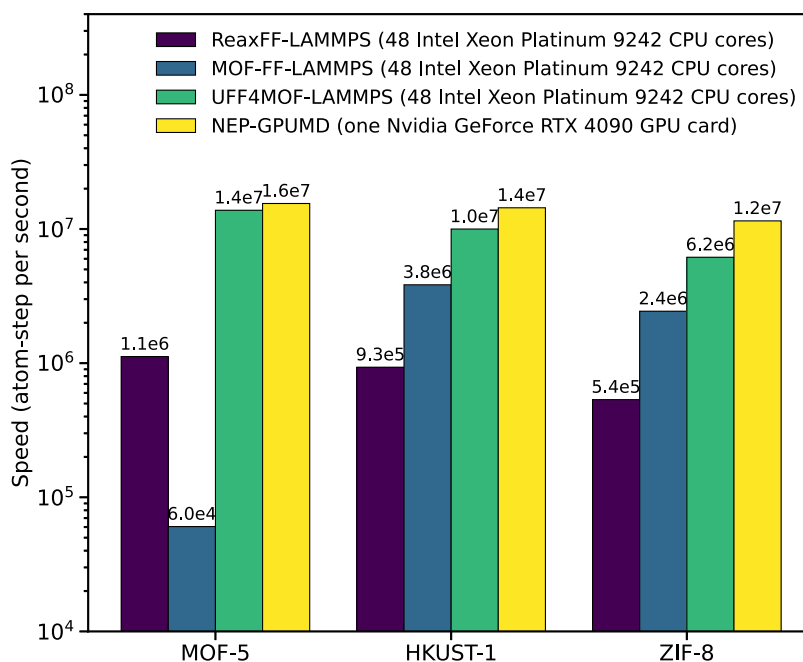

Figure 3. Computational speeds of the NEP models as implemented in GPUMD[44] (version 3.7, running with an Nvidia GeForce RTX 4090 GPU card) and several existing force fields as implemented in LAMMPS[34] (version 28 Mar 2023, running with 48 Intel Xeon Platinum 9242 CPU cores) for the three MOFs. The benchmark was performed using a 5 × 5 × 5 supercell containing 53,000, 78,000, and 34,500 atoms for MOF-5, HKUST-1, and ZIF-8, respectively.

Our NEP models not only achieve high accuracy but also have high computational efficiency. As can be seen from Figure 3, the NEP models as implemented in GPUMD[44] running with a single Nvidia GeForce RTX 4090 GPU card are faster than all of the existing force fields as implemented in LAMMPS[34] running with 48 Intel Xeon Platinum 9242 CPU cores. The MOF-FF force field for MOF-5[48] is particularly slow because it evaluates the Coulomb potential using the expensive Ewald summation. Apart from this, the computational speed of MOF-FF is higher than that of ReaxFF and lower than that of UFF4MOF.

Thermal Transport in MOFs. After confirming the reliability of our NEP models in MD simulations, we apply them to calculate the thermal conductivity using the various MD methods as reviewed in the Methods Section. In Figure 4, we show the HNEMD and EMD results for the three MOFs at 300 K and zero pressure obtained by using a supercell with 5 × 5 × 5 conventional cells. In both methods, the thermal conductivity has converged with respect to the production or correlation time. The results from the two methods are consistent, as expected, based on their physical equivalence.[45] However, we note that even if the total production time we
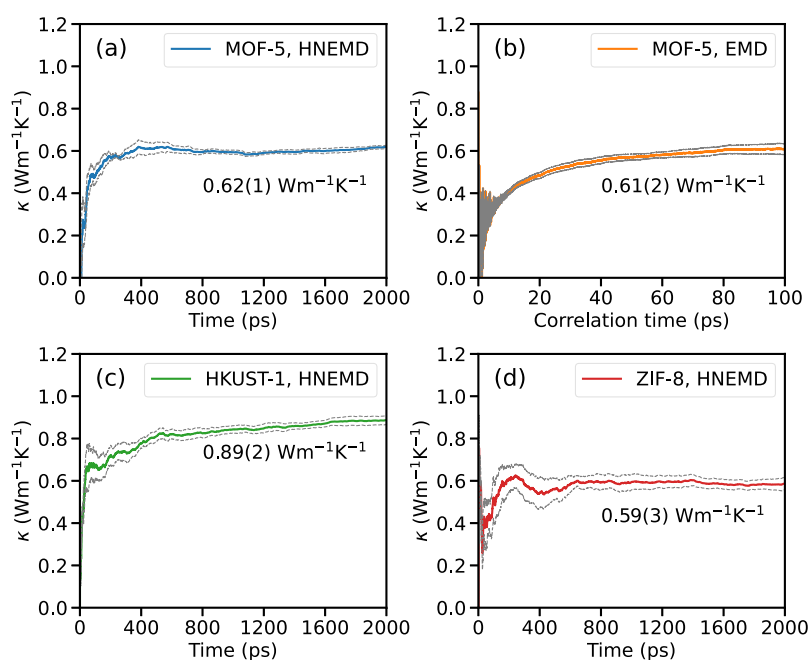
Figure 4. Cumulative average of the thermal conductivity as calculated using the HNEMD method for (a) MOF-5, (c) HKUST-1, and (d) ZIF-8 at 300 K. (b) Running thermal conductivity as calculated using the EMD method for MOF-5. The simulation cells contain $5 \times 5 \times 5$ conventional cells. In each panel, the middle line represents the average, and the other two represent the upper and lower bounds, as calculated from five independent runs.

used for the EMD method for each system (50 ns) is much larger than that for the HNEMD method (10 ns), the latter still has smaller statistical errors, which demonstrates the superior computational efficiency of the HNEMD method.[45]

In both the HNEMD and the EMD methods, periodic boundary conditions are applied in the three directions, and the results are regarded as those for infinitely large systems. However, this requires eliminating the finite-size effects by using a sufficiently large supercell. While previous works often assumed that a supercell with $2 \times 2 \times 2$ conventional cells is sufficient to obtain convergent results in EMD simulations,[12−14,17,19,20,36] our results in Figure 5 show that for all of the three MOFs, a supercell with $5 \times 5 \times 5$ conventional cells is required to converge the thermal conductivity. Note that agreement between the HNEMD and the EMD methods
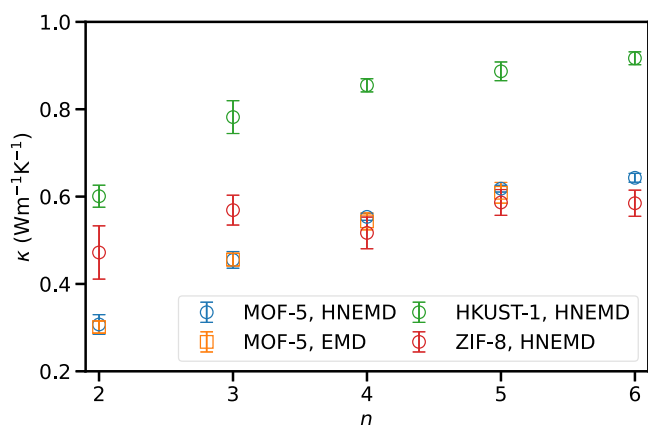
for MOF-5 is confirmed for all of the simulation domains up to the $5 \times 5 \times 5$ supercell.

Several studies have predicted a weak temperature dependence of the thermal conductivity of MOF-5[12] and various ZIF materials, such as ZIF-8,[13,19] ZIF-4,[25] and ZIF-62,[25] using a small supercell in EMD simulations. With the small $2 \times 2 \times 2$ supercell, we also obtained a weak temperature dependence of the thermal conductivity of MOF-5, as shown in Figure 6 and Table 1. Particularly, the thermal conductivity is almost constant from 300 to 400 K. However, using the converged $5 \times 5 \times 5$ supercell, a notable temperature dependence of $\sim T^{-0.6}$ is obtained. This again highlights the importance of

Figure 5. Thermal conductivity κ as a function of the number of conventional cells n in one direction of a cubic supercell for the three MOFs at 300 K from the HNEMD and EMD (for MOF-5 only) simulations.

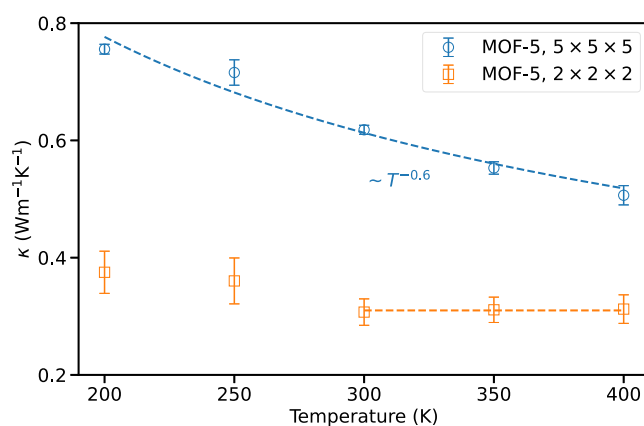**Figure 6.** Thermal conductivity κ as a function of temperature for MOF-5 as obtained by using the $5 \times 5 \times 5$ and $2 \times 2 \times 2$ supercells. The dashed line for the case of a $5 \times 5 \times 5$ supercell indicates a $\sim T^{-0.6}$ fitting, and the dashed line for the case of a $2 \times 2 \times 2$ supercell indicates that the thermal conductivity is a constant from 300 to 400 K.

Table 1. Thermal Conductivities (in Units of W/(m K)) of MOF-5 Calculated by Using the HNEMD Method with Different Supercell Sizes at Different Temperatures[a]

supercells	200 K	250 K	300 K	350 K	400 K
$2 \times 2 \times 2$	0.38(4)	0.36(4)	0.31(2)	0.31(2)	0.31(2)
$5 \times 5 \times 5$	0.76(1)	0.72(2)	0.62(1)	0.55(1)	0.51(2)

[a]The numbers within the parentheses are statistical uncertainties for the last significant number.

using a sufficiently large supercell in EMD and HNEMD simulations.

The calculated thermal conductivity values at 300 K using the converged $5 \times 5 \times 5$ supercell are listed in Table 2. Our

Table 2. Thermal Conductivities (in Units of W/(m K)) of the Three MOFs Calculated by Using the HNEMD Method and EMD Method (for MOF-5 Only) with Different Supercell Sizes (the Number of Conventional Cells n in One Direction of a Cubic Supercell) at 300 K[a]

	EMD	HNEMD		
n	MOF-5	MOF-5	HKUST-1	ZIF-8
2	0.30(1)	0.31(2)	0.60(3)	0.47(6)
3	0.46(2)	0.46(2)	0.78(4)	0.57(3)
4	0.54(2)	0.55(1)	0.86(2)	0.52(4)
5	0.61(2)	0.62(1)	0.89(2)	0.59(3)
6		0.64(1)	0.92(2)	0.59(3)

[a]The numbers within the parentheses are statistical uncertainties for the last significant number.

Figure 7. Spectral thermal conductivity $\kappa(\omega)$ as a function of phonon frequency $\omega/2\pi$ for (a) MOF-5, (b) HKUST-1, and (c) ZIF-8 at 300 K calculated by using different supercell sizes.

predicted thermal conductivity of ZIF-8, 0.59 ± 0.03 W/(m K), closely matches with the experimentally measured value of 0.64 ± 0.09 W/(m K).[10] For HKUST-1, our predicted thermal conductivity, 0.89 ± 0.02 W/(m K), is only slightly larger than the experimentally measured value of 0.69 ± 0.05 W/(m K).[11] For these two MOFs, good agreement with experiments is achieved for the first time. In the case of MOF-5, we predicted a thermal conductivity of 0.62 ± 0.01 W/(m K), which is significantly higher than the experimentally measured value of 0.32 W/(m K).[7] This discrepancy is yet to be understood, and we will discuss it further below.

The finite-size effects can be understood in terms of spectral thermal conductivity, as shown in Figure 7. With a larger simulation domain size, phonons with longer wavelengths (smaller frequencies) are brought into existence, which contribute significantly in the low-frequency region. Figure 7 shows that the contribution from phonons with $\omega/2\pi < 1$ THz is significantly reduced when the small $2 \times 2 \times 2$ supercell is used. To understand this more quantitatively, we note that the phonon group velocities for the acoustic branches are about 5 km/s, based on the spectral energy density shown in Figure 8. Taking MOF-5 as an example, the largest phonon wavelength that can exist in a $2 \times 2 \times 2$ supercell is about 5 nm, and the frequency for it is about 1 THz. That is, phonons with frequencies smaller than 1 THz are largely suppressed in this supercell. With a $5 \times 5 \times 5$ supercell, phonons with $\omega/2\pi < 1$ THz can be activated, and their contribution to the total thermal conductivity is almost converged. In all three MOFs, phonons with $\omega/2\pi < 1$ THz contribute about 50% to the total thermal conductivity.

The large spectral thermal conductivities in the low-frequency region are associated with the large phonon MFPs,
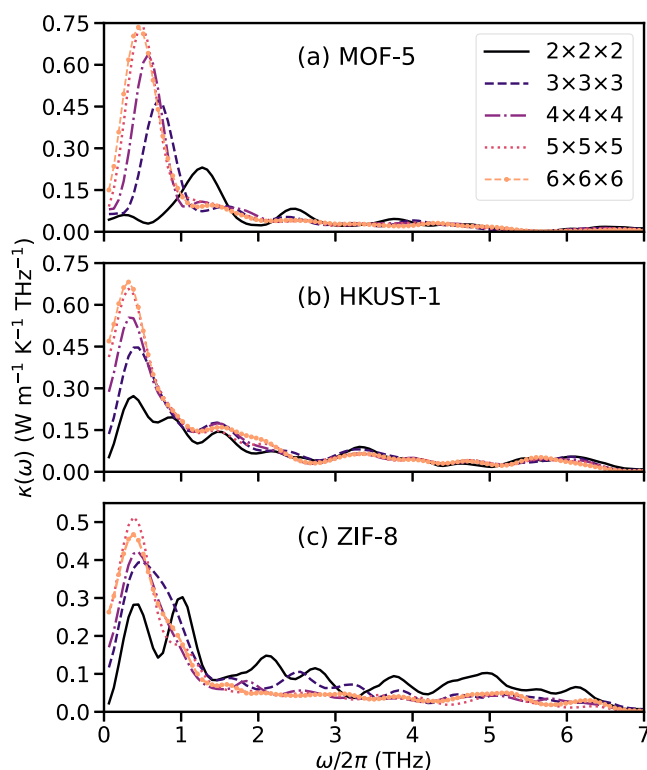
as shown in Figure 9. The maximum phonon MFPs for MOF-5, HKUST-1, and ZIF-8 are 0.17, 0.28, and 0.16 μm, respectively. Due to the large MFPs, the apparent thermal conductivity only saturates in the micrometer scale of system length L, as shown in the inset of Figure 9. The slow convergence of the thermal conductivity with respect to L for HKUST-1 is further confirmed by independent NEMD simulations.

Using a MOF-FF potential, Wieser et al.[23,26] observed that the thermal conductivity of MOF-5 is not converged up to 20 nm in NEMD simulations, which is consistent with our results. This means that the large phonon MFPs in MOFs are not sensitive to the details of the interatomic potential. As we have discussed above, the large phonon MFPs in the low-frequency region mean that a $2 \times 2 \times 2$ supercell is not sufficient to obtain converged thermal conductivity in EMD simulations. With this small supercell, our EMD prediction of 0.30(1) W/(m K) is very close to the experimental value[7] of 0.32 W/(m K) as well as the previous EMD simulations.[12] However, this good agreement is most likely an accident, as the thermal conductivity predicted by our EMD simulations with a $5 \times 5 \times 5$ supercell is 0.61 ± 0.02 W/(m K), which is about twice the experimental value. A possible explanation of the discrepancy between our predictions and the previous experiment[7] is that the measured samples might not be single crystals. According to the length-scaling in the inset of Figure 9, the thermal conductivity of MOF-5 is only about half of the converged value when L is about 0.1 μm. We therefore speculate that the experimental samples[7] might be nanocrystals with a characteristic size of 0.1 μm or contain defects that have been observed to significantly reduce the thermal conductivity of MOFs.[18]
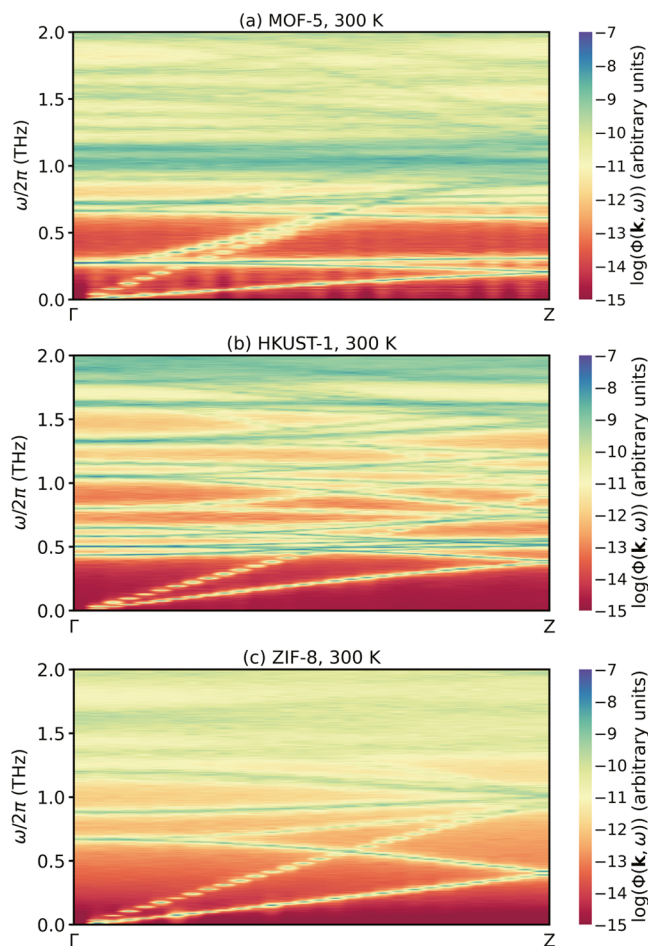
Figure 8. Phonon spectral energy density of (a) MOF-5, (b) HKUST-1, and (c) ZIF-8 at 300 K as a function of wave number in the $\Gamma-Z$ path and phonon frequency.

Figure 9. Phonon MFP $\lambda(\omega)$ as a function of phonon frequency $\omega/2\pi$ for the three MOFs at 300 K. Inset: Apparent thermal conductivity $\kappa(L)$ as a function of the transport length L for the three MOFs at 300 K as calculated from the HNEMD-based spectral decomposition method (lines) and direct NEMD simulations (markers; for HKUST-1 only).

SUMMARY AND CONCLUSIONS

In summary, we have developed a set of accurate and highly efficient MLPs for three typical MOFs, including MOF-5, HKUST-1, and ZIF-8, using the efficient NEP approach and quantum-mechanical DFT calculations. For each MOF, the NEP model accurately reproduces the radial distribution function and angular distribution function as compared to DFT calculations, showing much higher accuracy than typical empirical force fields. We have performed extensive MD simulations with the NEP models to study thermal transport in these MOFs. We have mainly used the HNEMD method but have also used the EMD and NEMD methods for cross-checking the consistency of the results.

We have carefully examined the finite-size effects in EMD and HNEMD simulations for which previous works have not paid sufficient attention. Contrary to the common assumption that a supercell with $2 \times 2 \times 2$ conventional cells is sufficient, our results indicate that at least a $5 \times 5 \times 5$ supercell is required to achieve converged results. This is not only relevant to the calculated thermal conductivity values at a specific temperature but also crucial for obtaining the correct temperature dependence of the thermal conductivity. Our results suggest that the thermal conductivities of MOFs exhibit a moderate temperature dependence of $\sim T^{-0.6}$, which is not as strong as $\sim T^{-1}$ in conventional crystals but is also not as weak as $\sim T^0$ in typical amorphous materials.
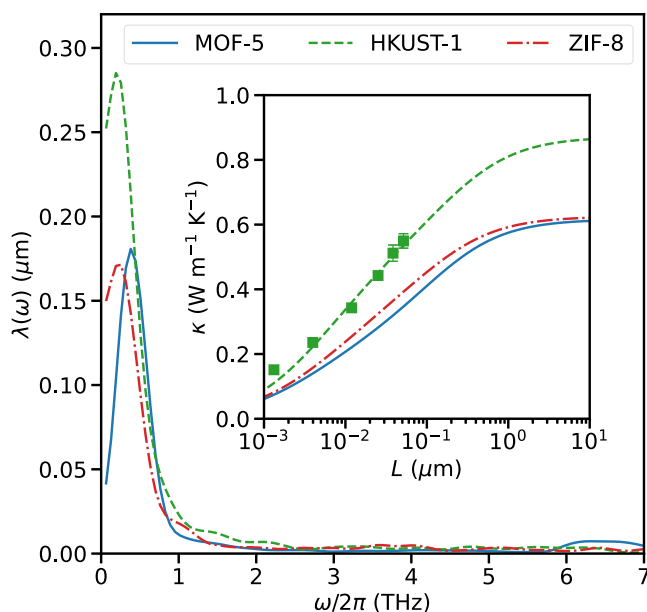
With the converged simulation cell size, we have obtained the spectral thermal conductivity within the HNEMD method and found that phonons with frequency $\omega/2\pi < 1$ THz contribute about half the total thermal conductivity. These phonons have sub-micrometer MFPs, which can neither be accessed by EMD simulations with a small supercell nor NEMD simulations with short domain lengths, making them largely undiscovered before.

Among the three MOFs we considered, HKUST-1 has the largest thermal conductivity, while the other two have smaller and comparable thermal conductivity. Our results for HKUST-1 and ZIF-8 are in very good agreement with experiments,[10,11] but the same has not been achieved for MOF-5.[7] More work is needed to resolve this discrepancy.

Overall, we have obtained a clear picture of thermal transport in MOFs. They typically have a thermal conductivity smaller than 1 W/(m K), but there are THz-phonons with sub-micrometer MFPs that contribute a significant portion of the thermal conductivity and give rise to a strong length dependence of the apparent thermal conductivity. Therefore, the thermal conductivity in nanocrystals can be heavily reduced compared to single crystals.

METHODS

NEP Approach. In the NEP approach, a feedforward neural network (NN) with a single hidden layer of N_{neu} neurons is used to represent the site energy U_i of atom i as a function of a descriptor vector with N_{des} components[41]

$$U_i = \sum_{\mu=1}^{N_{\text{neu}}} w_\mu^{(1)} \tanh\left(\sum_{\nu=1}^{N_{\text{des}}} w_{\mu\nu}^{(0)} q_\nu^i - b_\mu^{(0)} \right) - b^{(1)} \tag{1}$$

where $\tanh(x)$ is the activation function, $\mathbf{w}^{(0)}$, $\mathbf{w}^{(1)}$, $\mathbf{b}^{(0)}$, and $b^{(1)}$ are the trainable weight and bias parameters in the NN. The atomic environment descriptor q_ν^i consists of a number of radial and angular components similar to the Behler–Parrinello approach.[57] The radial

descriptor components (with a cutoff radius r_c^R) only depend on atom-pair distances and are constructed based on Chebyshev polynomials. The angular descriptor components (with a cutoff radius r_c^A) also depend on angular information and are constructed based on spherical harmonics similar to the atomic cluster expansion approach.[58] A NEP model is trained using the separable natural evolution strategy (SNES)[59] by minimizing a loss function that is defined as a weighted sum of the RMSEs of energy, force, and virial as well as terms serving as l_1 and l_2 regularization. For more details of the NEP approach, we refer to the literature.[41−43]

There are a number of important hyperparameters in the NEP approach that need to be carefully chosen. Based on previous publications[41−43] and our extensive tests, we reached a set of optimized hyperparameters for the three MOFs. For all three MOFs, we used the same hyperparameters except for the cutoff radius of the angular descriptor components r_c^A that was set to 4 Å for both MOF-5 and HKUST-1 but to 3 Å for ZIF-8. The cutoff radius of the radial descriptor components was set to a larger value of 6 Å to incorporate more neighbors. Both the radial and angular descriptor components have radial functions. For the radial descriptor components, we used 13 radial functions, each being a linear combination of 13 Chebyshev polynomials. For the angular descriptor components, we used 9 radial functions, each being a linear combination of 9 Chebyshev polynomials. For the angular descriptor components, we used both three-body and four-body correlations up to degree $l = 4$ and $l = 2$, respectively, in the spherical harmonics Y_{lm}. The number of neurons in the hidden layer was chosen to be $N_{neu} = 80$, which is large enough to achieve a high accuracy.

Reference Data Generation. We employed an iterative scheme, as shown in Figure S1, to construct the training data for the NEP model of each material. While a more sophisticated method is needed for complex materials with very large primitive cells,[60] it is feasible to generate the training data using the primitive cells in our case. Starting from the optimized structure of the primitive cell of a given material, we performed constant-volume DFT-driven MD simulations with the target temperature linearly increasing from 10 to 800 K within 10 ps (10,000 steps) and sampled 560 structures. We also generated 100 structures by applying random cell deformations (−3 to 3%) and atomic displacements (within 0.1 Å) starting from the optimized structure. We performed more accurate DFT calculations (see below) for the 660 structures and obtained the initial data set and trained the first NEP model. Then, we performed NEP-driven MD simulations at our intended thermodynamic conditions and selected 100 more structures based on the farthest-point sampling by comparing the distance of structures in two-dimensional (2D) principal component (PC) space. We then trained the second NEP model based on the expanded 760 structures. Another round of expansion was similarly performed, and our final data set has 860 structures for each material. We have used 90% for training and 10% for testing.

The DFT-MD simulations were conducted in the isothermal (NVT) ensemble with an energy threshold of 10^{-5} eV, an energy cutoff of 520 eV for the electronic self-consistent loop, and the Γ point was sampled in the Brillouin zone. To obtain the energy, force, and virial data for NEP training, we performed DFT calculations using the Perdew−Burke−Ernzerhof functional[61] and the projector-augmented wave method[62] implemented in Vienna Ab initio Simulation Package.[63,64] We sampled the Brillouin zone with a k-point density of 0.2/Å and used Gaussian smearing with a width of 0.05 eV. For the electronic self-consistent loop, we set a threshold of 10^{-7} eV with an energy cutoff of 600 eV.

HNEMD Method and Spectral Conductivity in the Diffusive Regime. The HNEMD method has been shown to be one of the most efficient MD methods for obtaining diffusive thermal transport properties.[45] In HNEMD simulation of thermal conduction in solid, an external driving force

$$F_i^{ext} = F_e \cdot W_i \tag{2}$$

is added to each atom i to drive the system out of equilibrium. Here, W_i is the virial tensor of atom i, and F_e is the driving force parameter, which is of the dimension of inverse length. The driving force will induce a net heat current J whose ensemble average (represented by $\langle \cdots \rangle$ below) is proportional to the driving force parameter

$$\frac{\langle J^\alpha \rangle}{TV} = \sum_\beta \kappa^{\alpha\beta} F_e^\beta \tag{3}$$

where T is the system temperature, V is the system volume, and $\kappa^{\alpha\beta}$ is the $\alpha\beta$-component of the thermal conductivity tensor. For explicit expressions of the virial tensor and heat current vector applicable to the NEP model, we refer to the literature.[35,41,43] In this paper, the three MOFs have cubic symmetry, and without loss of generality, we can focus on the diagonal component in the x direction, giving

$$\kappa^{xx} = \frac{\langle J^x \rangle}{TVF_e^x} \tag{4}$$

The magnitude of the driving force parameter F_e needs to be small enough to keep the system within the linear-response regime but also large enough to induce a sufficiently large signal-to-noise ratio. We have tested that for all of the three MOFs, $F_e^x = 2 \times 10^{-4}$/Å is an appropriate value for temperatures ≥300 K, while a slightly smaller value of $F_e^x = 1.5 \times 10^{-4}$/Å is more appropriate for lower temperatures.

An appealing feature of the HNEMD method is that the thermal conductivity can be spectrally decomposed[45]

$$\kappa^{xx} = \int_0^\infty \frac{d\omega}{2\pi} \kappa^{xx}(\omega) \tag{5}$$

where

$$\kappa^{xx}(\omega) = \frac{2}{VTF_e^x} \int_{-\infty}^\infty dt e^{i\omega t} K^x(t) \tag{6}$$

Here, $K^x(t)$ is the x-component of the virial-velocity correlation function

$$K(t) = \sum_i \langle W_i(0) \cdot v_i(t) \rangle \tag{7}$$

where v_i is the velocity of atom i.

NEMD Method and Spectral Conductance in the Ballistic Regime. With the HNEMD method alone, one can only access the diffusive transport properties. To obtain a more complete description of thermal transport from ballistic to diffusive, an established efficient scheme[45,65] is to supplement HNEMD with NEMD simulations.

In our NEMD simulations, two local thermostats, i.e., heat source and heat sink, at different temperatures, are used to generate a nonequilibrium steady state with constant heat flux. The thermal conductance G between the two thermostats separated by distance L can be calculated as

$$G^{xx}(L) = \frac{J^x}{\Delta TV} \tag{8}$$

where ΔT is the temperature difference between the heat source and the heat sink. An effective thermal conductivity (also called apparent thermal conductivity) $\kappa^{xx}(L)$ for the finite system with a transport length of L can be defined as[65]

$$\kappa^{xx}(L) = G^{xx}(L)L = \frac{J^x}{(\Delta T/L)V} \tag{9}$$

Similar to thermal conductivity, the thermal conductance can also be spectrally decomposed

$$G^{xx}(L) = \int_0^\infty \frac{d\omega}{2\pi} G^{xx}(L, \omega) \tag{10}$$

where

$$G^{xx}(L, \omega) = \frac{2}{V\Delta T} \int_{-\infty}^\infty dt e^{i\omega t} K^x(t) \tag{11}$$

The limit of zero transport length $L \to 0$ corresponds to the ballistic limit $G_b^{xx}(\omega) = G^{xx}(L \to 0, \omega)$, and one can define a spectrally

decomposed MFP as $\lambda^{xx}(\omega) = \kappa^{xx}(\omega)/G_b^{xx}(\omega)$. With the spectral MFP, we can obtain the spectral thermal conductivity with any transport length

$$\kappa^{xx}(L, \omega) = \frac{\kappa^{xx}(\omega)}{1 + \lambda^{xx}(\omega)/L} \qquad (12)$$

and the integrated thermal conductivity

$$\kappa^{xx}(L) = \int_0^\infty \frac{d\omega}{2\pi} \kappa^{xx}(L, \omega) \qquad (13)$$

EMD Method. In the EMD method based on a Green–Kubo relation,[31,32] the xx-component of the running thermal conductivity can be expressed as an integral of the heat current auto-correlation function

$$\kappa^{xx}(t) = \frac{1}{k_B T^2 V} \int_0^t dt' \langle J^x(0)J^x(t') \rangle \qquad (14)$$

where k_B is Boltzmann's constant and t is the upper limit of the correlation time.

Phonon Spectral Energy Density Calculations. We perform the phonon spectral energy density[66,67] calculations to examine the phonon dispersion structures of MOFs. The phonon spectral energy density is a function of wave vector ($\boldsymbol{k}$) and frequency (ω) and can be calculated using the following formula in MD simulations

$$\Phi(\boldsymbol{k}, \omega) = \frac{1}{4\pi\tau_0 N} \sum_\alpha^{\{x,y,z\}} \sum_b^B m_b \times$$

$$\left| \int_0^{\tau_0} \sum_{n_{x,y,z}}^N v_\alpha \binom{n_{x,y,z}}{b}; t \right) \times \exp\left[i\boldsymbol{k} \cdot \boldsymbol{r} \binom{n_{x,y,z}}{0} - i\omega t \right] dt \bigg|^2 \qquad (15)$$

where τ_0 is the total simulation time, N is the number of unit cells in the crystal, b is the atom label in a given unit cell n, m_b is the mass of atom b in the unit cell, $n_{x,y,z}$ is the index number of unit cells along the x, y, and z directions, $v_\alpha \binom{n_{x,y,z}}{b}; t$ denotes the velocity of atom b of the n-th unit cell along the α direction at time t, and $\boldsymbol{r}\binom{n_{x,y,z}}{0}$ is the equilibrium position of unit cell n.

Details of the MD Simulations. We used the GPUMD package (version 3.7)[44] to perform all of the MD simulations. A time step of 0.5 fs was used with the velocity Verlet integration scheme, which has been confirmed to be small enough. The time coupling parameter in the thermostat and barostat are 50 fs and 500 fs, respectively. In all HNEMD, EMD, and NEMD simulations, we calculated the statistical error of the thermal conductivity as the standard error of the mean values from five independent runs.

HNEMD Simulations. In HNEMD simulations, we first equilibrated for 100 ps in the isothermal-isobaric (NpT) ensemble at a given target temperature and zero pressure, followed by a 2 ns production stage in the NVT ensemble. The NpT ensemble was achieved by the Berendsen method.[68] The NVT ensemble was achieved by the Nose–Hoover chain thermostat.[69] The external driving force was added during the production stage.

Note that the HNEMD method does not involve a temperature gradient, although there is nonzero macroscopic heat flux circulating in the system. Therefore, the "temperature profile" is uniform in HNEMD. According to the linear-response theory, the time needed to reach a steady state in HNEMD is comparable to the correlation time in the EMD method, which is of the order of 100 ps, as can be seen from Figure 4b. Each HNEMD simulation was carried up to 20,000 ps, and the thermal conductivity was sampled well within steady states.

NEMD Simulations. In NEMD simulations, the system was only periodic in the lateral directions, and the two ends in the transport direction were fixed. Next to one fixed end, a heat source region with a temperature of 325 K was created by applying a Langevin

thermostat[70] and a heat sink region with a temperature of 275 K was similarly created next to the other fixed end. The thermostated regions contain two conventional cells in the transport direction, which are sufficiently long to avoid artifacts.[65] After an equilibration similar to the HNEMD simulation, the NEMD simulation with the two local Langevin thermostats was performed for 1 ns. All of the simulated samples have 5×5 conventional cells in the lateral directions, and the lengths in the transport direction are varied to explore different transport regimes.

EMD Simulations. In EMD simulations, after an equilibration similar to the HNEMD simulation, a production run in the micro-canonical (NVE) ensemble was performed for 10 ns. We relied on human inspection for estimating the convergence of the Green–Kubo integral. For all three MOFs, the Green–Kubo integral has fully converged up to a correlation time of 80 ps [see Figure 4b]. We have used the $\kappa(t)$ values from 80 to 100 ps to calculate a mean value for each independent run.

Phonon Spectral Energy Density Calculations. For the phonon spectral energy density calculations, we used a $1 \times 1 \times 60$ supercell for each MOF. All systems were first relaxed in the NVT ensemble for 0.5 ns, followed by a 0.75 ns production stage in the NVE ensemble. The velocities and positions of all atoms during the final 0.5 ns were collected to calculate the spectral energy density.

■ ASSOCIATED CONTENT

Data Availability Statement

The source code and documentation for gpumd are available at https://github.com/brucefan1983/GPUMD and https://gpumd.org, respectively. The source code for spectral energy density calculations is available at https://github.com/Tingliangstu/pySED. The training and testing results for the NEP models are freely available at https://gitlab.com/brucefan1983/nep-data. Representative input and output files for thermal conductivity calculations are freely available at https://github.com/hityingph/supporting-info.

Supporting Information

The Supporting Information is available free of charge at https://pubs.acs.org/doi/10.1021/acsami.3c07770.

> Workflow for NEP construction; lattice constants at zero temperature; and parity plots and RMSEs of energy; force; and virial (PDF)

■ AUTHOR INFORMATION

Corresponding Authors

Penghua Ying — *School of Science, Harbin Institute of Technology, Shenzhen 518055, P. R. China;* orcid.org/0000-0002-5758-2369; Email: hityingph@163.com

Zheyong Fan — *College of Physical Science and Technology, Bohai University, Jinzhou 121013, P. R. China;* orcid.org/0000-0002-2253-8210; Email: brucenju@gmail.com

Authors

Ting Liang — *Department of Electronic Engineering and Materials Science and Technology Research Center, The Chinese University of Hong Kong, Shatin, N.T., Hong Kong SAR 999077, P. R. China*

Ke Xu — *Department of Physics, Xiamen University, Xiamen 361005, P. R. China;* orcid.org/0000-0001-5254-5297

Jin Zhang — *School of Science, Harbin Institute of Technology, Shenzhen 518055, P. R. China;* orcid.org/0000-0002-7032-4399

Jianbin Xu — *Department of Electronic Engineering and Materials Science and Technology Research Center, The Chinese University of Hong Kong, Shatin, N.T., Hong Kong*

SAR 999077, P. R. China; ● orcid.org/0000-0003-0509-9508

Zheng Zhong − *School of Science, Harbin Institute of Technology, Shenzhen 518055, P. R. China;* ● orcid.org/0000-0001-5293-7098

Complete contact information is available at:
https://pubs.acs.org/10.1021/acsami.3c07770

Notes
The authors declare no competing financial interest.

■ REFERENCES

(1) Rowsell, J. L.; Yaghi, O. M. Metal−organic Frameworks: A New Class of Porous Materials. *Microporous Mesoporous Mater.* **2004**, *73*, 3−14.

(2) Yaghi, O. M.; O'Keeffe, M.; Ockwig, N. W.; Chae, H. K.; Eddaoudi, M.; Kim, J. Reticular Synthesis and the Design of New Materials. *Nature* **2003**, *423*, 705−714.

(3) Li, B.; Wen, H.-M.; Zhou, W.; Chen, B. Porous Metal−Organic Frameworks for Gas Storage and Separation: What, How, and Why? *J. Phys. Chem. Lett.* **2014**, *5*, 3468−3479.

(4) Hanikel, N.; Prévot, M. S.; Yaghi, O. M. MOF Water Harvesters. *Nat. Nanotechnol.* **2020**, *15*, 348−355.

(5) Stassen, I.; Burtch, N.; Talin, A.; Falcaro, P.; Allendorf, M.; Ameloot, R. An Updated Roadmap for the Integration of Metal−Organic Frameworks with Electronic Devices and Chemical Sensors. *Chem. Soc. Rev.* **2017**, *46*, 3185−3241.

(6) Rogge, S. M. J.; Bavykina, A.; Hajek, J.; Garcia, H.; Olivos-Suarez, A. I.; Sepúlveda-Escribano, A.; Vimont, A.; Clet, G.; Bazin, P.; Kapteijn, F.; Daturi, M.; Ramos-Fernandez, E. V.; Llabrés i Xamena, F. X.; Van Speybroeck, V.; Gascon, J. Metal−Organic and Covalent Organic Frameworks as Single-Site Catalysts. *Chem. Soc. Rev.* **2017**, *46*, 3134−3184.

(7) Huang, B.; Ni, Z.; Millward, A.; McGaughey, A.; Uher, C.; Kaviany, M.; Yaghi, O. Thermal Conductivity of a Metal-Organic Framework (MOF-5): Part II. Measurement. *Int. J. Heat Mass Transfer* **2007**, *50*, 405−411.

(8) Ming, Y.; Purewal, J.; Liu, D.; Sudik, A.; Xu, C.; Yang, J.; Veenstra, M.; Rhodes, K.; Soltis, R.; Warner, J.; Gaab, M.; Müller, U.; Siegel, D. J. Thermophysical Properties of MOF-5 Powders. *Microporous Mesoporous Mater.* **2014**, *185*, 235−244.

(9) Huang, J.; Xia, X.; Hu, X.; Li, S.; Liu, K. A General Method for Measuring the Thermal Conductivity of MOF Crystals. *Int. J. Heat Mass Transfer* **2019**, *138*, 11−16.

(10) Huang, J.; Fan, A.; Xia, X.; Li, S.; Zhang, X. In Situ Thermal Conductivity Measurement of Single-Crystal Zeolitic Imidazolate Framework-8 by Raman-Resistance Temperature Detectors Method. *ACS Nano* **2020**, *14*, 14100−14107.

(11) Babaei, H.; DeCoster, M. E.; Jeong, M.; Hassan, Z. M.; Islamoglu, T.; Baumgart, H.; McGaughey, A. J. H.; Redel, E.; Farha, P. E.; Hopkins, O. K.; Malen, J. A.; Wilmer, C. E. Observation of Reduced Thermal Conductivity in a Metal-Organic Framework Due to the Presence of Adsorbates. *Nat. Commun.* **2020**, *11*, No. 4010.

(12) Huang, B.; McGaughey, A.; Kaviany, M. Thermal Conductivity of Metal-Organic Framework 5 (MOF-5): Part I. Molecular Dynamics Simulations. *Int. J. Heat Mass Transfer* **2007**, *50*, 393−404.

(13) Zhang, X.; Jiang, J. Thermal Conductivity of Zeolitic Imidazolate Framework-8: A Molecular Simulation Study. *J. Phys. Chem. C* **2013**, *117*, 18441−18447.

(14) Han, L.; Budge, M.; Greaney, P. A. Relationship Between Thermal Conductivity and Framework Architecture in MOF-5. *Comput. Mater. Sci.* **2014**, *94*, 292−297.

(15) Babaei, H.; Wilmer, C. E. Mechanisms of Heat Transfer in Porous Crystals Containing Adsorbed Gases: Applications to Metal-Organic Frameworks. *Phys. Rev. Lett.* **2016**, *116*, No. 025902.

(16) Wieme, J.; Vandenbrande, S.; Lamaire, A.; Kapil, V.; Vanduyfhuys, L.; Van Speybroeck, V. Thermal Engineering of Metal−Organic Frameworks for Adsorption Applications: A Molecular Simulation Perspective. *ACS Appl. Mater. Interfaces* **2019**, *11*, 38697−38707.

(17) Sørensen, S. S.; Østergaard, M. B.; Stepniewska, M.; Johra, H.; Yue, Y.; Smedskjaer, M. M. Metal−Organic Framework Glasses Possess Higher Thermal Conductivity Than Their Crystalline Counterparts. *ACS Appl. Mater. Interfaces* **2020**, *12*, 18893−18903.

(18) Islamov, M.; Babaei, H.; Wilmer, C. E. Influence of Missing Linker Defects on the Thermal Conductivity of Metal−Organic Framework HKUST-1. *ACS Appl. Mater. Interfaces* **2020**, *12*, 56172−56177.

(19) Ying, P.; Zhang, J.; Zhang, X.; Zhong, Z. Impacts of Functional Group Substitution and Pressure on the Thermal Conductivity of ZIF-8. *J. Phys. Chem. C* **2020**, *124*, 6274−6283.

(20) Ying, P.; Zhang, J.; Zhong, Z. Effect of Phase Transition on the Thermal Transport in Isoreticular DUT Materials. *J. Phys. Chem. C* **2021**, *125*, 12991−13001.

(21) Cheng, R.; Li, W.; Wei, W.; Huang, J.; Li, S. Molecular Insights into the Correlation between Microstructure and Thermal Conductivity of Zeolitic Imidazolate Frameworks. *ACS Appl. Mater. Interfaces* **2021**, *13*, 14141−14149.

(22) Lamaire, A.; Wieme, J.; Hoffman, A. E.; Van Speybroeck, V. Atomistic Insight in the Flexibility and Heat Transport Properties of the Stimuli-Responsive Metal−Organic Framework MIL-53 (Al) for Water-Adsorption Applications Using Molecular Simulations. *Faraday Discuss.* **2021**, *225*, 301−323.

(23) Wieser, S.; Kamencek, T.; Dürholt, J. P.; Schmid, R.; Bedoya-Martínez, N.; Zojer, E. Identifying the Bottleneck for Heat Transport in Metal−Organic Frameworks. *Adv. Theory Simul.* **2021**, *4*, No. 2000211.

(24) Zhou, Y.; Huang, B.; Cao, B.-Y. Vibrational Modes with Long Mean Free Path and Large Volumetric Heat Capacity Drive Higher Thermal Conductivity in Amorphous Zeolitic Imidazolate Framework-4. *Mater. Today Phys.* **2021**, *21*, No. 100516.

(25) Zhou, Y.; Xu, Y.; Gao, Y.; Volz, S. Origin of the Weakly Temperature-Dependent Thermal Conductivity in ZIF-4 and ZIF-62. *Phys. Rev. Mater.* **2022**, *6*, No. 015403.

(26) Wieser, S.; Kamencek, T.; Schmid, R.; Bedoya-Martínez, N.; Zojer, E. Exploring the Impact of the Linker Length on Heat Transport in Metal−Organic Frameworks. *Nanomaterials* **2022**, *12*, No. 2142.

(27) Fan, H.; Yang, C.; Zhou, Y. Ultralong Mean Free Path Phonons in HKUST-1 and Their Scattering by Water Adsorbates. *Phys. Rev. B: Condens. Matter Mater. Phys.* **2022**, *106*, No. 085417.

(28) Li, H.; Eddaoudi, M.; O'Keeffe, M.; Yaghi, O. M. Design and Synthesis of an Exceptionally Stable and Highly Porous Metal-Organic Framework. *Nature* **1999**, *402*, 276−279.

(29) Huang, X.-C.; Lin, Y.-Y.; Zhang, J.-P.; Chen, X.-M. Ligand-Directed Strategy for Zeolite-Type Metal−Organic Frameworks: Zinc (II) Imidazolates with Unusual Zeolitic Topologies. *Angew. Chem., Int. Ed.* **2006**, *45*, 1557−1559.

(30) Chui, S. S.-Y.; Lo, S. M.-F.; Charmant, J. P.; Orpen, A. G.; Williams, I. D. A Chemically Functionalizable Nanoporous Material [Cu3 (TMA) 2 (H2O) 3] N. *Science* **1999**, *283*, 1148−1150.

(31) Green, M. S. Markoff Random Processes and the Statistical Mechanics of Time-Dependent Phenomena. II. Irreversible Processes in Fluids. *J. Chem. Phys.* **1954**, *22*, 398−413.

(32) Kubo, R. Statistical-Mechanical Theory of Irreversible Processes. I. General Theory and Simple Applications to Magnetic and Conduction Problems. *J. Phys. Soc. Jpn.* **1957**, *12*, 570−586.

(33) Stukowski, A. Visualization and Analysis of Atomistic Simulation Data with OVITO−The Open Visualization Tool. *Modell. Simul. Mater. Sci. Eng.* **2009**, *18*, No. 015012.

(34) Thompson, A. P.; Aktulga, H. M.; Berger, R.; Bolintineanu, D. S.; Brown, W. M.; Crozier, P. S.; in't Veld, P. J.; Kohlmeyer, A.; Moore, S. G.; Nguyen, T. D.; Shan, R.; Stevens, M. J.; Tranchida, J.; Trott, C.; Plimpton, S. J. LAMMPS-A Flexible Simulation Tool for Particle-Based Materials Modeling at the Atomic, Meso, and Continuum Scales. *Comput. Phys. Commun.* **2022**, *271*, No. 108171.

(35) Fan, Z.; Pereira, L. F. C.; Wang, H.-Q.; Zheng, J.-C.; Donadio, D.; Harju, A. Force and Heat Current Formulas for Many-Body Potentials in Molecular Dynamics Simulations with Applications to Thermal Conductivity Calculations. *Phys. Rev. B* **2015**, *92*, No. 094301.

(36) Wei, W.; Huang, J.; Li, W.; Peng, H.; Li, S. Impacts of Ethanol and Water Adsorptions on Thermal Conductivity of ZIF-8. *J. Phys. Chem. C* **2019**, *123*, 27369−27374.

(37) Tayfuroglu, O.; Kocak, A.; Zorlu, Y. A Neural Network Potential for the IRMOF Series and its Application for Thermal and Mechanical Behaviors. *Phys. Chem. Chem. Phys.* **2022**, *24*, 11882−11897.

(38) Vandenhaute, S.; Cools-Ceuppens, M.; DeKeyser, S.; Verstraelen, T.; Van Speybroeck, V. Machine Learning Potentials for Metal-Organic Frameworks Using an Incremental Learning Approach. *npj Comput. Mater.* **2023**, *9*, No. 19.

(39) Achar, S. K.; Wardzala, J. J.; Bernasconi, L.; Zhang, L.; Johnson, J. K. Combined Deep Learning and Classical Potential Approach for Modeling Diffusion in UiO-66. *J. Chem. Theory Comput.* **2022**, *18*, 3593−3606.

(40) Zheng, B.; Oliveira, F. L.; Ferreira, R. N. B.; Steiner, M.; Hamann, H.; Gu, G. X.; Luan, B. Quantum Informed Machine-Learning Potentials for Molecular Dynamics Simulations of CO2's Chemisorption and Diffusion in Mg-MOF-74. *ACS Nano* **2023**, *17*, 5579−5587.

(41) Fan, Z.; Zeng, Z.; Zhang, C.; Wang, Y.; Song, K.; Dong, H.; Chen, Y.; Ala-Nissila, T. Neuroevolution Machine Learning Potentials: Combining High Accuracy and Low Cost in Atomistic Simulations and Application to Heat Transport. *Phys. Rev. B* **2021**, *104*, No. 104309.

(42) Fan, Z. Improving the Accuracy of the Neuroevolution Machine Learning Potential for Multi-Component Systems. *J. Phys.: Condens. Matter* **2022**, *34*, No. 125902.

(43) Fan, Z.; Wang, Y.; Ying, P.; Song, K.; Wang, J.; Wang, Y.; Zeng, Z.; Xu, K.; Lindgren, E.; Rahm, J. M.; Gabourie, A. J.; Liu, J.; Dong, H.; Wu, J.; Chen, Y.; Zhong, Z.; Sun, J.; Erhart, P.; Su, Y.; Ala-Nissila, T. GPUMD: A Package for Constructing Accurate Machine-Learned Potentials and Performing Highly Efficient Atomistic Simulations. *J. Chem. Phys.* **2022**, *157*, No. 114801.

(44) Fan, Z.; Chen, W.; Vierimaa, V.; Harju, A. Efficient Molecular Dynamics Simulations with Many-Body Potentials on Graphics Processing Units. *Comput. Phys. Commun.* **2017**, *218*, 10−16.

(45) Fan, Z.; Dong, H.; Harju, A.; Ala-Nissila, T. Homogeneous Nonequilibrium Molecular Dynamics Method for Heat Transport and Spectral Decomposition with Many-Body Potentials. *Phys. Rev. B* **2019**, *99*, No. 064308.

(46) Addicoat, M. A.; Vankova, N.; Akter, I. F.; Heine, T. Extension of the Universal Force Field to Metal−Organic Frameworks. *J. Chem. Theory Comput.* **2014**, *10*, 880−891.

(47) Boyd, P. G.; Moosavi, S. M.; Witman, M.; Smit, B. Force-Field Prediction of Materials Properties in Metal-Organic Frameworks. *J. Phys. Chem. Lett.* **2017**, *8*, 357−363.

(48) Pallach, R.; Keupp, J.; Terlinden, K.; Frentzel-Beyme, L.; Kloß, M.; Machalica, A.; Kotschy, J.; Vasa, S. K.; Chater, P. A.; Sternemann, C.; et al. Frustrated Flexibility in Metal-Organic Frameworks. *Nat. Commun.* **2021**, *12*, No. 4097.

(49) Bureekaew, S.; Amirjalayer, S.; Tafipolsky, M.; Spickermann, C.; Roy, T. K.; Schmid, R. MOF-FF − A Flexible First-Principles Derived Force Field for Metal-Organic Frameworks. *Phys. Status Solidi (B)* **2013**, *250*, 1128−1141.

(50) Dürholt, J. P.; Fraux, G.; Coudert, F.-X.; Schmid, R. Ab Initio Derived Force Fields for Zeolitic Imidazolate Frameworks: MOF-FF for ZIFs. *J. Chem. Theory Comput.* **2019**, *15*, 2420−2432.

(51) Monti, S.; Li, C.; Carravetta, V. Reactive Dynamics Simulation of Monolayer and Multilayer Adsorption of Glycine on Cu (110). *J. Phys. Chem. C* **2013**, *117*, 5221−5228.

(52) Han, S. S.; Choi, S.-H.; Van Duin, A. C. Molecular Dynamics Simulations of Stability of Metal−Organic Frameworks against H 2 O using the ReaxFF Reactive Force Field. *Chem. Commun.* **2010**, *46*, 5713−5715.

(53) Yang, Y.; Shin, Y. K.; Li, S.; Bennett, T. D.; Van Duin, A. C.; Mauro, J. C. Enabling Computational Design of ZIFs using ReaxFF. *J. Phys. Chem. B* **2018**, *122*, 9616−9624.

(54) van Duin, A. C. T.; Dasgupta, S.; Lorant, F.; Goddard, W. A. ReaxFF: A Reactive Force Field for Hydrocarbons. *J. Phys. Chem. A* **2001**, *105*, 9396−9409.

(55) Wang, B.; Ying, P.; Zhang, J. Effects of Missing Linker Defects on the Elastic Properties and Mechanical Stability of the Metal−Organic Framework HKUST-1. *J. Phys. Chem. C* **2023**, *127*, 2533−2543.

(56) Castel, N.; Coudert, F.-X. Atomistic Models of Amorphous Metal−Organic Frameworks. *J. Phys. Chem. C* **2022**, *126*, 6905−6914.

(57) Behler, J.; Parrinello, M. Generalized Neural-Network Representation of High-Dimensional Potential-Energy Surfaces. *Phys. Rev. Lett.* **2007**, *98*, No. 146401.

(58) Drautz, R. Atomic Cluster Expansion for Accurate and Transferable Interatomic Potentials. *Phys. Rev. B* **2019**, *99*, No. 014104.

(59) Lanzi, P. L.; Schaul, T.; Schaul, T.; Glasmachers, T.; Schmidhuber, J. In *High Dimensions and Heavy Tails for Natural Evolution Strategies*, Proceedings of the 13th Annual Conference on Genetic and Evolutionary Computation; ACM, 2011; pp 845−852.

(60) Eckhoff, M.; Behler, J. From Molecular Fragments to the Bulk: Development of a Neural Network Potential for MOF-5. *J. Chem. Theory Comput.* **2019**, *15*, 3793−3809.

(61) Perdew, J. P.; Burke, K.; Ernzerhof, M. Generalized Gradient Approximation Made Simple. *Phys. Rev. Lett.* **1996**, *77*, 3865−3868.

(62) Blöchl, P. E. Projector Augmented-Wave Method. *Phys. Rev. B* **1994**, *50*, No. 17953.

(63) Kresse, G.; Furthmüller, J. Efficient Iterative Schemes for Ab Initio Total-Energy Calculations Using a Plane-Wave Basis Set. *Phys. Rev. B* **1996**, *54*, No. 11169.

(64) Kresse, G.; Joubert, D. From Ultrasoft Pseudopotentials to the Projector Augmented-Wave Method. *Phys. Rev. B* **1999**, *59*, 1758−1775.

(65) Li, Z.; Xiong, S.; Sievers, C.; Hu, Y.; Fan, Z.; Wei, N.; Bao, H.; Chen, S.; Donadio, D.; Ala-Nissila, T. Influence of Thermostatting on Nonequilibrium Molecular Dynamics Simulations of Heat Conduction in Solids. *J. Chem. Phys.* **2019**, *151*, No. 234105.

(66) Thomas, J. A.; Turney, J. E.; Iutzi, R. M.; Amon, C. H.; McGaughey, A. J. H. Predicting Phonon Dispersion Relations and Lifetimes from the Spectral Energy Density. *Phys. Rev. B* **2010**, *81*, No. 081411.

(67) Feng, T.; Qiu, B.; Ruan, X. Anharmonicity and Necessity of Phonon Eigenvectors in the Phonon Normal Mode Analysis. *J. Appl. Phys.* **2015**, *117*, No. 195102.

(68) Berendsen, H. J. C.; Postma, J. P. M.; Van Gunsteren, W. F.; DiNola, A.; Haak, J. R. Molecular Dynamics with Coupling to an External Bath. *J. Chem. Phys.* **1984**, *81*, 3684−3690.

(69) Tuckerman, M. *Statistical Mechanics: Theory and Molecular Simulation*; Oxford University Press, 2010; Chapter 4, pp 188−199.

(70) Bussi, G.; Parrinello, M. Accurate Sampling Using Langevin Dynamics. *Phys. Rev. E* **2007**, *75*, No. 056707.